

# A high-efficiency plug-and-play superconducting qubit network

Michael Mollenhauer,<sup>1,\*</sup> Abdullah Irfan,<sup>1,\*</sup> Xi Cao,<sup>1,\*</sup> Supriya Mandal,<sup>1</sup> and Wolfgang Pfaff<sup>1,2,†</sup>

<sup>1</sup>*Department of Physics, University of Illinois at Urbana-Champaign, Urbana, IL 61801, USA*

<sup>2</sup>*Materials Research Laboratory, University of Illinois at Urbana-Champaign, Urbana, IL 61801, USA*

Modular architectures are a promising approach to scale quantum devices to the point of fault tolerance and utility [1–3]. Modularity is particularly appealing for superconducting qubits, as monolithically manufactured devices are limited in both system size and quality [4–6]. Constructing complex quantum systems as networks of interchangeable modules can overcome this challenge through ‘Lego-like’ assembly, reconfiguration, and expansion, in a spirit similar to modern classical computers. First prototypical superconducting quantum device networks have been demonstrated [7–18]. Interfaces that simultaneously permit interchangeability and high-fidelity operations remain a crucial challenge, however. Here, we demonstrate a high-efficiency interconnect based on a detachable cable between superconducting qubit devices. We overcome the inevitable loss in a detachable connection through a fast pump scheme, enabling inter-module SWAP efficiencies at the 99%-level in less than 100 ns. We use this scheme to generate high-fidelity entanglement and operate a distributed logical dual-rail qubit. At the observed  $\sim 1\%$  error rate, operations through the interconnect are at the threshold for fault-tolerance. These results introduce a modular architecture for scaling quantum processors with reconfigurable and expandable networks.

## I. INTRODUCTION

At the core of a modular device architecture lies the interchangeability of subsystems. Assembly from interchangeable components is routine in classical computers, and has been recognized also as a key scaling approach for quantum processors [1–4]. For one, seamless addition and removal of components enables system upgrades with pre-tested, higher-fidelity qubit modules. Second, expansion of system size and computational power can be achieved simply by plugging in additional modules (Fig. 1a). Because manufactured devices inevitably have finite yield and fluctuating parameters, it is difficult to realize monolithic quantum systems containing large numbers of high-quality qubits; This is a particularly important challenge in solid-state systems, such as superconducting qubits. Modular quantum computing architectures can thus be key for overcoming a central challenge in realizing large-scale quantum processors [4–6].

Achieving this vision of modular scaling hinges critically on efficient interchangeable interconnects. Previous works have accepted compromises in network capability or performance due to the difficulty in combining low loss and interchangeability. Recent examples include tolerating sparse weak links [19]; performing measurement-based protocols in which entanglement is realized non-deterministically [7–9]; or achieving low loss by sacrificing plug-and-play interchangeability using wafer- or wire-bonding [11–13, 20, 21]. In contrast, fully embracing modularity as a key scaling strategy requires inter-module links on par with intra-module gates, with deterministic operations at the 1% error level [22, 23] between interchangeable modules. Losses in experiments to date

exceed 15% [14–18], however, well in excess of requirements for scaling.

Here, we introduce a high-efficiency modular architecture for interchangeable superconducting quantum devices. We have developed an interconnect between separately packaged transmon qubits that combines a reliably (un)pluggable coaxial-cable link with fast and high-fidelity Raman transitions. Using this architecture, we demonstrate inter-module SWAP gates with  $\sim 1\%$  loss in under 100 ns. Remarkably, our interconnect rivals the performance shown with superconducting bonds between qubit circuits and cables [11–13]. The speed and efficiency of our pump scheme further enables the generation of high-fidelity inter-module entanglement, and the operation of a distributed dual-rail qubit. Our interconnect does not require any circuit elements beyond the intrinsic nonlinearity of the qubits, making it applicable for different types of qubits beyond the transmon.

## II. INTERCONNECT DESIGN

A quantum interconnect scheme should combine low loss with flexibility in assembly and connectivity. The latter makes cable-based connections highly attractive. Additionally, superconducting coaxial cables can be used as a low-loss transmission line resonator [10–14, 24], allowing their use as an off-chip version of a quantum bus [25]. Realizing a detachable connection between qubit and cable implies a capacitive coupling scheme as illustrated in Figure 1b. To achieve reliable yet interchangeable connectivity, we have designed a connector mechanism that yields quality factors for a demountable bus made of Al cable of up to  $Q_b \approx 500,000$  (Fig. 5c). Here, we have mounted the connector to a sub-cutoff waveguide containing a fixed-frequency transmon [26]. This design is readily compatible with leading, hardware-efficient approaches to quantum error correction based on high- $Q$

\* These authors contributed equally.

† [wpfaff@illinois.edu](mailto:wpfaff@illinois.edu)

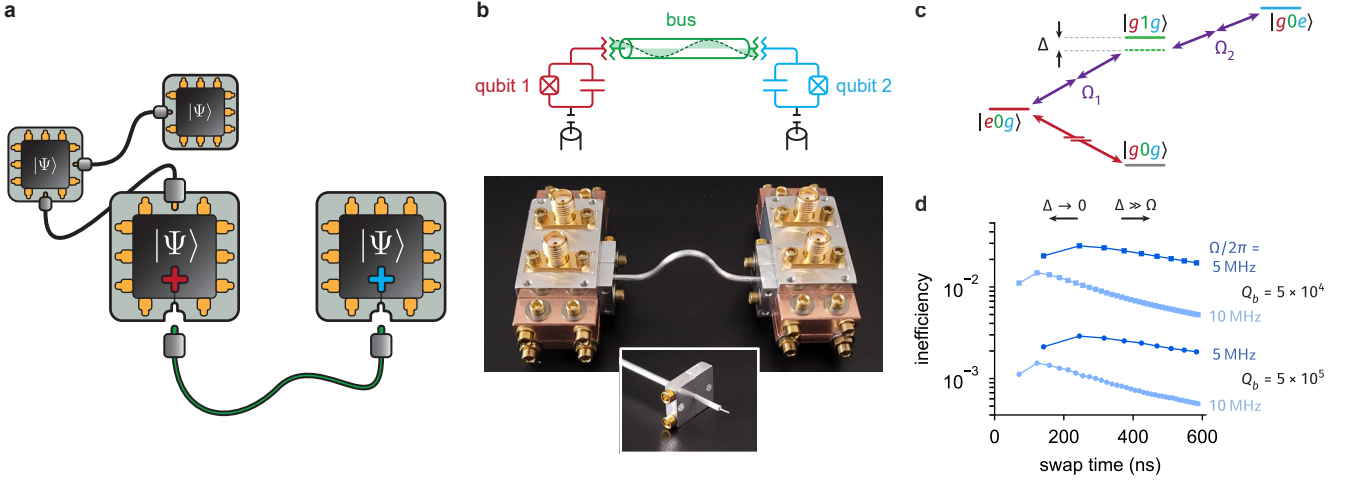


**FIG. 1. Experiment overview.** **a**, Scaling quantum devices as a network of modules permits reconfiguration or replacement of subsystems. The minimal requirement is the ability to transmit quantum states with high fidelity between qubits in different modules (shown as blue and red crosses) through detachable links (shown as green cable). **b**, Experimental implementation of a ‘plug-and-play’ quantum network. A superconducting coaxial cable with custom connectors couples capacitively to transmon qubits and acts as a modular, high- $Q$  quantum bus. Here: a 73 mm cable, with the  $2\lambda$  mode acting as the bus. Both qubits and their readout resonators are on separate chips, packaged in separate housings. **c**, Sketch of the level diagram and drive scheme for Raman transitions through the bus. Pumping each transmon separately realizes two-photon sideband transitions (purple arrows) between qubits (red and blue levels) and bus mode (green). Qubit-qubit swaps are realized for  $\Omega_1 = \Omega_2 \equiv \Omega$ . **d**, Simulated inefficiency of a swap from qubit 1 to qubit 2 as a function of the swap time, assuming ideal qubits. Squares and circles:  $Q_b = 50,000$  (as shown for NbTi cables [14]) and  $Q_b = 500,000$  (Al cables, see Appendix A 1), respectively. Dark and light curves:  $\Omega/2\pi = 5$  MHz and 10 MHz, respectively. Shorter times are realized with small detunings (leftmost points:  $\Delta = 0$ ), longer times are in the detuned Raman regime.

cavities [27–33], for which a modular scaling paradigm is particularly attractive [34].

To complete the interconnect, the physical link must be combined with a compatible, high-fidelity gate scheme. The capacitive coupling between cable and qubit comes with two important consequences we need to consider: First, the attainable cable  $Q$  is reduced compared to what has been shown with galvanically bonded cable connections; second, it precludes the use of fast tunable couplers based on flux-tuning [11–13]. To realize a sufficiently fast gate, we target a Raman-type process [14] by parametrically driving sideband transitions between the qubits and bus mode (Fig. 1c). Fixed-frequency transmon qubits allow for driving such transitions natively [35]. In order to realize gate speeds that strongly exceed interconnect loss rates we have designed a low-frequency driving scheme that enables fast sideband rates without introducing excess decoherence (see below, and Appendix B 1).

To assess the performance of the interconnect scheme we consider the efficiency of a SWAP gate between distant qubits. Executing high-fidelity SWAPs is sufficient for executing inter-module circuits in a network of multi-qubit modules [11]. The performance of the targeted SWAP is determined by the following key factors. Loss in the bus leads to inefficiency that can be counteracted by introducing a detuning [36]. This comes at the cost of slower speeds, which in turn leads to inefficiency due to finite qubit coherence. Figure 1d shows predictions for

how  $\sim 1\%$ -level SWAP inefficiency can be reached (Appendix C 1), leading us to the following strategy. Generally,  $\Omega$  should be as high as possible. Because we must anticipate that cable coupling has a detrimental effect on the qubit, we prioritize speed to avoid inefficiency from qubit decoherence. As shown in Figure 1d, high  $Q_b$  and fast sidebands predict excitation swaps with sub-percent loss in around 100 ns, much faster than currently achievable transmon coherence times.

### III. QUBIT-BUS SIDEBANDS

At the heart of the targeted Raman process are sideband transitions that convert qubit excitations into bus photons, and that can be tuned up individually for each module. To realize these transitions, the connector is designed such that a mode of the bus resonator is coupled to both qubits in the dispersive regime [37]. Sidebands can then be driven by applying a pump tone to the transmon, with a frequency  $\omega_i = (|\omega_b - \omega_{a,i}|)/2$ , where  $\omega_b$  and  $\omega_{a,i}$  are the resonant frequencies of target bus mode and qubit  $i$ , respectively. This can be understood as degenerate four-wave mixing, for which we predict sidebands that are faster than the more commonly employed non-degenerate case (Appendix B 1). The system is designed such that  $\omega_i$  is placed several GHz below transmon and bus (Appendix A 1) and thus strongly detuned from any

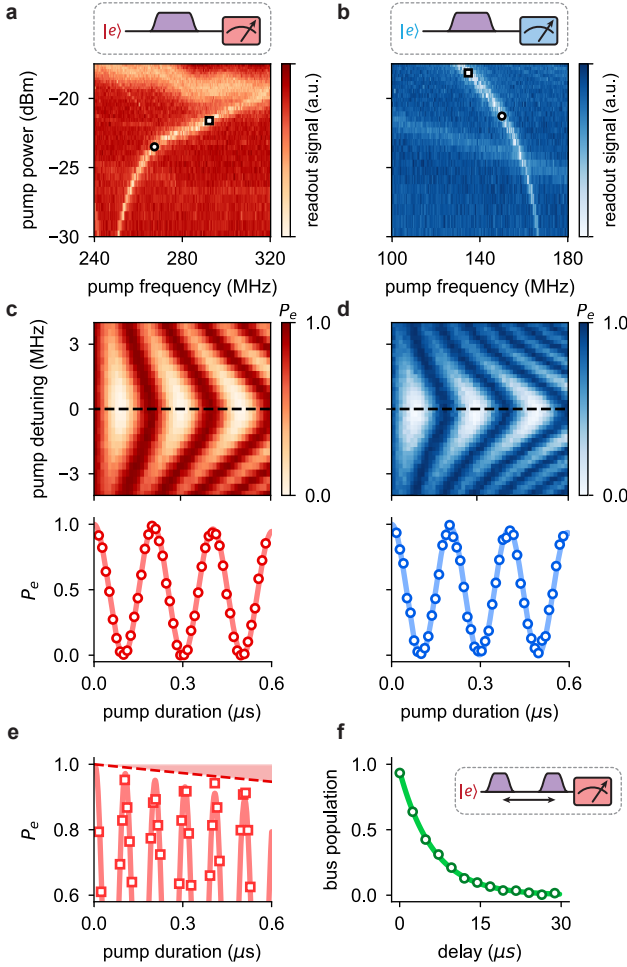


FIG. 2. **Fast sidebands between qubit and high- $Q$  detachable bus.** **a, b,** Readout signal of the left (red) and right (blue) qubits as a function of pump frequency and device input power. Circle and square markers along the sideband resonance indicate  $\Omega_i/2\pi = 5$  MHz and 10 MHz, respectively. **c, d,** Top: Time evolution of the excited state population,  $P_e$ , of qubits 1 (red) and 2 (blue) during pumping with  $\Omega_i/2\pi = 5$  MHz. Bottom: Linecuts at zero detuning. Lines are a model taking into account  $\Omega_i$  and undriven decoherence rates of qubit and bus mode. **e,** Excited state population from a fit to sideband oscillations measured on qubit 1 with  $\Omega_1/2\pi = 10$  MHz. Red shaded region shows the limit based on undriven decoherence rates. **f,** Measurement of the single-photon decay of the bus mode. Fit to an exponential decay yields a lifetime of  $\tau = 6.2$   $\mu$ s.

excitable mode. Near resonance, the Hamiltonian describing the process is  $H_{sb,i} = (\Omega_i/2)(e^{i\Delta t}\hat{a}_i^\dagger\hat{b} + \text{h.c.})$ , where  $\hat{a}$  and  $\hat{b}$  are the annihilation operators for transmon  $i$  and bus mode, and the sideband rate  $\Omega_i$  is set by the pump strength.

We begin by calibrating the sidebands for both qubits individually. To find  $\omega_i$ , we first prepared each qubit in the excited state and recorded its change in state as a function of the frequency and power after applying a pump tone of fixed length (Fig. 2a,b). Tuning the

pump to resonance and compensating for Stark shifts (Appendix B 2), rapid oscillations between the  $|e0\rangle$  and  $|g1\rangle$  states are induced, where the oscillation frequency  $\Omega$  is set by the pump power. Figure 2c,d shows ‘sideband Rabi’ oscillations for the case where  $\Omega_{1,2}/2\pi$  is tuned to 5 MHz. Importantly, we find that the decay of these oscillations can be explained by the undriven loss rates of qubit and cable alone, indicating that the strong pump does not cause excess decoherence.

Our simple model predicts that the sideband rate  $\Omega$  can be increased simply by increasing pump power, thus speeding up the transition. Larger rates can, however, come at the cost of additional loss. As an example, Figure 2e shows 10 MHz oscillations obtained for qubit 1. Their decay is visibly faster than predictions from undriven loss rates, obtained from qubit coherence as well as the in-situ determined bus loss (Fig. 2f). The onset of excess loss varies between devices, suggesting that mechanisms such as drive-induced leakage [38] or coupling to random two-level fluctuators [39] play a role in setting the speed limit. In our experiment we have been able to reliably obtain ‘clean’ 5 MHz oscillations; in the following we show that they enable low-loss inter-module excitation transfer.

#### IV. INTER-DEVICE GATES

Having tuned up individual sidebands, we have next turned them on simultaneously to realize a Raman transition between the qubits. Our sideband rates and bus- $Q$  predict a fast and high-efficiency SWAP for  $\Delta = 0$  (Fig. 1d). From the in-situ determined  $Q_b = 2.0 \times 10^5$  (Fig. 2f) we predict a 0.97% swap inefficiency for  $\Omega_{1,2}/2\pi = 5$  MHz, taking into account bus loss as well as qubit decoherence. To test this prediction, we have prepared qubit 1 in  $|e\rangle$ , and applied both pumps at the same time. After compensating for small inter-chip Stark-shifts (Appendix C 2), we have observed high-visibility oscillations in agreement with dynamics predicted by the total Hamiltonian,  $H = H_{sb,1} + H_{sb,2}$ , and established decoherence rates (Fig. 3a). The oscillation period is, as expected,  $2\sqrt{2}\pi/\Omega$ , and fitting the dynamics yields a loss per swap of 1.0(1)%, in quantitative agreement with our model (Appendix C 2).

To benchmark the achievable loss per gate, we have performed pulsed SWAP gates. Because we drive sidebands with a second-order process, this mode of operation requires care in the pulse shaping to avoid excess errors (Appendix C 2) [40]. Applying smoothed flat-top pulses with a length of 142 ns, we have been able to achieve stroboscopic excitation swaps that match the quality of the continuous evolution (Fig. 3b). The loss per gate can be inferred by fitting the accumulated error as a function of number of swaps to an exponential decay (Fig. 3c), yielding a loss rate of 1.2(1)% per SWAP-gate; the excess error can be explained by tune-up imperfections (Fig. 7 and Fig. 8). We have repeated

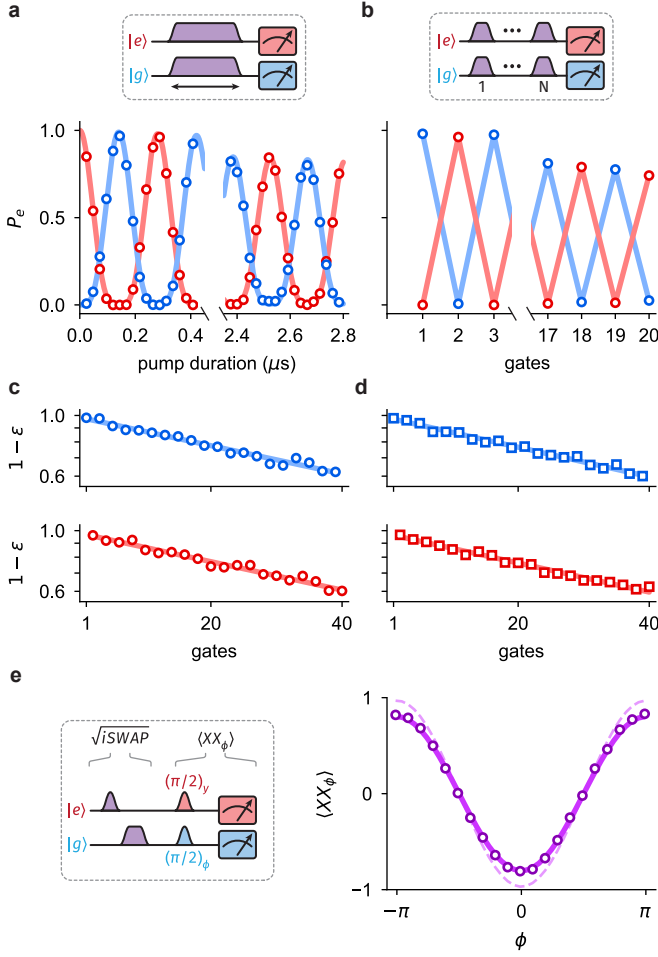


FIG. 3. **Inter-module swaps.** **a**, Measured excited state populations after applying the pump for a variable time;  $\Omega/2\pi = 5$  MHz. Solid line: model based on independently determined decoherence properties of (undriven) qubits and bus. **b**, Measured excited state population after applying discrete SWAP gates. **c**, **d**, Total accumulated error as a function of number of SWAPs on qubits 1 (red) and 2 (blue) for  $\Omega/2\pi = 5$  MHz and gate time 142 ns (left panel) and  $\Omega/2\pi = 10$  MHz and gate time 70 ns (right panel). **e**, Inter-module entanglement realized in a stroboscopic approach, verified by measuring  $\langle XX_\phi \rangle$ . Dots: raw data, not corrected for state preparation and measurement (SPAM) errors. Dashed line: simulation based on independently determined decoherence rates, not taking SPAM errors into account. Solid line: simulation with SPAM errors. Without SPAM, computed Bell state fidelity is 0.974.

the same procedure also with the sidebands tuned to  $\Omega_{1,2}/2\pi = 10$  MHz; while the gate time drops to 70 ns in this case, the loss rate remains the same due to drive-induced excess errors discussed above (Fig. 3d). This inefficiency of order 1% in a sub-100 ns SWAP gate is a central benchmark result of our experiment, demonstrating a high-efficiency inter-device link.

Besides transferring population, the Raman transition needs to preserve phase coherence. From the near-perfect

agreement of time-dynamics with our model (Fig. 7), coherence is already evident. It can be shown more explicitly, however, by measuring transversal correlations after generating entanglement using the Raman process. Fast sidebands and the high  $Q$  of the bus enable us to generate inter-module entanglement in a simple, stroboscopic fashion. We have first prepared qubit 1 in  $|e\rangle$ , then swapped half the population into the bus, followed by swapping the full bus population to qubit 2. This routine corresponds to performing a  $\sqrt{\text{iSWAP}}$  entangling gate. To analyze the expected entangled state,  $(|eg\rangle + |ge\rangle)/\sqrt{2}$ , we have measured the correlator  $\langle XX_\phi \rangle$ , where  $X_\phi$  is an operator rotated by  $\phi$  with respect to  $X$  (Fig. 3e). The data is in quantitative agreement with a simulation that only takes into account the undriven loss of all modes, predicting a Bell state fidelity of 97.4%. In this approach, the bus is populated for a significant time, explaining excess loss compared to the SWAP; this loss could, however, be suppressed with detuned Raman transitions.

## V. DETUNED RAMAN REGIME

During a Raman transition with  $\Delta \gg \Omega_{1,2}$  the bus is populated only ‘virtually’ and bus loss is suppressed (Fig. 4a) [36]. The coherent evolution of an excitation occurs then in the two-dimensional subspace spanned by the states  $|eg\rangle$  and  $|ge\rangle$ ; the rf-driven sidebands realize arbitrary rotations of this effective two-level system. This amounts to operating a distributed dual-rail qubit (Fig. 4b) [42] — a logical encoding that has recently garnered attention in the context of hardware-efficient quantum error correction with superconducting circuits [32, 41, 43]. Reaching this detuned regime requires sidebands that are fast compared to loss rates. The combination of low-loss interconnect and fast sideband transitions uniquely allows us to access this regime in a modularly connected network, providing a path toward loss-resilient entanglement and the operation of distributed logical qubits.

To demonstrate the capability to control the network in this fashion, we have first realized Rabi oscillations in the subspace  $\{|0\rangle_L \equiv |eg\rangle, |1\rangle_L \equiv |ge\rangle\}$ . Following preparation in  $|eg\rangle$ , we have applied detuned sideband drives with  $\Delta/\Omega \approx 5$ . In this regime, the time evolution of the system is governed by the effective Hamiltonian  $H \approx (\Omega_R/2)(\hat{a}_1^\dagger \hat{a}_2 e^{i\delta t} + \text{h.c.})$ , predicting oscillations with Rabi frequency  $\Omega_R = \Omega^2(2\Delta - \delta)/2[\Delta(\Delta - \delta)]$ , where  $\delta$  is a relative detuning between the pumps (Fig. 4a). Figure 4c shows the characteristic chevron pattern obtained by measuring the time-dependent populations of both qubits, showing dynamics that are in quantitative agreement with numerical predictions. Importantly, we have observed oscillations that are still much faster than effective loss rates. The swap period shown here is, despite operating in a strongly detuned regime, on the sub-microsecond scale. At the half-swap time, corresponding to a  $\pi/2$  pulse of the dual-rail qubit, the two physical



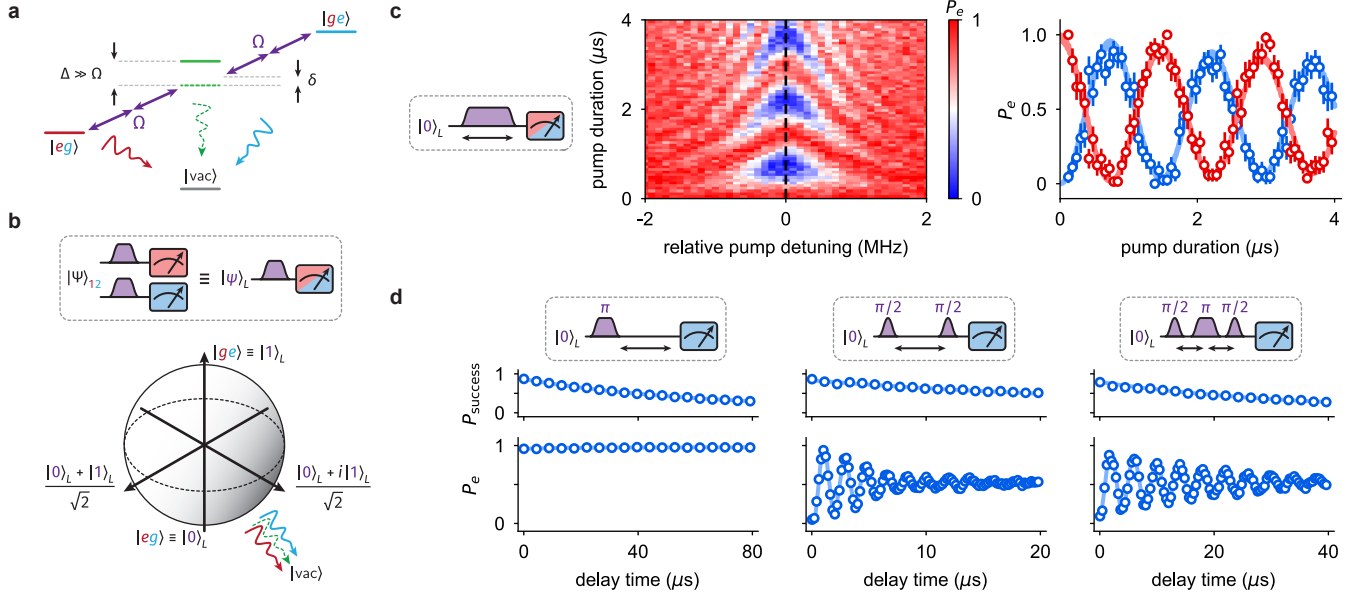


FIG. 4. **Dual-rail operations in the detuned Raman regime.** **a**, Energy level schematic. Sidebands are applied off-resonantly w.r.t. the bus mode and may be relatively detuned by  $\delta$ . Loss from the bus (green dashed arrow) can be suppressed at the cost of speed. **b**, Bloch sphere representation of the dual rail encoding. Photon loss relaxes the system into the vacuum, outside the qubit subspace. **c**, Time evolution of the qubit excited state populations (red: qubit 1; blue: qubit 2). Right panel: line cut at zero relative detuning. Line: model taking into account independently characterized decoherence parameters; the only free parameter is  $\Omega$ . **d**, Basic operations in the dual-rail subspace. After each sequence, both qubits are measured; events where both outcomes are  $g$  are discarded. Top panels: fraction of measurement results,  $P_{\text{success}}$ , that were not discarded. Bottom panels: Logical  $T_1$ ,  $T_{2R}$  and  $T_{2E}$  measurements (left to right), post-selected on success. Data points shown are probabilities of qubit 2 being excited; lines are fits.  $T_1$  is, as expected for a dual-rail encoding [41], practically infinite.  $T_2$  is limited by the individual qubits' coherence times.

qubits are in a maximally entangled Bell state. From the simulated time dynamics we estimate a Bell state fidelity of 0.98(1). While the effect of loss in the bus is suppressed compared to the resonant regime, fidelity is now limited by on-site decoherence.

Having observed high-contrast oscillations in the dual-rail subspace, we can next perform logical operations. Universal rotations can be executed by applying both pumps simultaneously with  $\delta = 0$  while controlling duration and phase. We demonstrate this in a proof-of-concept fashion by measuring the elementary coherence properties of the dual-rail qubit (Fig. 4d). A central feature of dual-rail qubits are erasure errors, as population loss relaxes the system to the vacuum outside the logical subspace. Here, we simply detect these erasures at the end of each experiment and eliminate them by postselection [41]. Our hardware could, however, be extended to perform mid-circuit erasure checks [43, 44] that would be required in an error correction code. While our simple demonstration does not have the biased errors required to lower the overhead for error correction [45], it provides an interesting perspective for logical qubit encodings in a distributed setting, and illustrates the potential for suppressing interconnect loss.

## VI. PERSPECTIVES

In summary, we have demonstrated a prototypical quantum network of interchangeable superconducting quantum devices. We have developed a high- $Q$  detachable quantum bus connection and combined it with a low frequency parametric pumping scheme to realize a high-efficiency interconnect at the 1% error level with operations on the order of 100 ns. Our drive scheme further enables the generation of high-fidelity entanglement and the operation of a distributed logical qubit. For practical reasons, we have employed a fairly short cable in our experiment. We note, however, that as long as  $\Omega$  is small compared to the free spectral range of the cable, no detrimental effects are expected, placing the length limit at the one-meter scale. Crucially, we find that the interconnect can be (re)attached with reproducible performance. System parameters fluctuate strongly between assembly cycles, which can be expected due to the simplicity of the mounting system; we have found, however, that fast sidebands can be achieved reliably (Fig. 9).

While the demonstrated performance and robustness of the interconnect is already highly promising for modular scaling, we anticipate that substantial improvements are possible by improving the mechanical design. The presented version of the connector hardware has a notice-

able impact on qubit coherence. A more mature design that preserves state-of-the-art coherence times [33, 46–49] would enable intermodule gate infidelities approaching  $10^{-3}$  (Fig. 1d). In this limit, operating on intermodule logical qubits would be on equal footing as intramodule operations, obviating the need for considering interconnects as weak links.

Our results pave the way for modular scaling of quantum processors. Transferring the interconnect hardware to more complex modules is readily achievable with existing technology. Importantly, the plug-and-play nature of our interconnect enables incremental changes to the network. This ability allows processor nodes to be added or replaced over time without compromising existing parts. The hardware design used in our work readily enables modular scaling of leading architectures for fault-tolerant quantum computing with bosonic encodings in high- $Q$  cavities [27–33]. While we have chosen a stripline-based architecture in our experiment, a qubit-to-cable coupling compatible with coplanar-waveguide (CPW) based processors may be realized by introducing antenna transitions [50, 51].

Finally, the simplicity of our interconnect scheme, not requiring specific coupler circuitry, makes it also appealing beyond transmon qubits. The only requirement for driving the sideband transitions is a suitable nonlinearity which can also be realized with other types of superconducting qubits such as the fluxonium [52, 53]. Additionally, we can envision high-fidelity interconnects between superconducting qubits and modalities that couple to superconducting resonators but have different environmental or packaging demands, such as spins [54, 55]. Our results thus establish a modular architecture for scalable homogeneous and heterogeneous quantum device networks.

## ACKNOWLEDGEMENTS

The research was carried out in part in the Materials Research Lab Central Facilities and the Holonyak Micro and Nanotechnology Lab at the University of Illinois. We thank K. Chow and R. Goncalves for help with fabrication; and B. DeMarco and A. Kou for critical reading of the manuscript. We acknowledge funding from the NSF Quantum Leap Challenge Institute for Hybrid Quantum Architectures and Networks (Award 2016136), from the IBM-Illinois Discovery Accelerator Institute, and the Army Research Office (Grant Number W911NF-23-1-0096). The views and conclusions contained in this document are those of the authors and should not be interpreted as representing the official policies, either expressed or implied, of the Army Research Office or the U.S. Government.

## AUTHOR CONTRIBUTIONS

M.M. designed the device. M.M., A.I., and X.C. developed the theory models, conducted the experiment, and analyzed the data. S.M., M.M. and A.I. developed and tested the sideband pumping scheme. The paper was written by M.M., A.I., X.C., and W.P., with comments from all authors. The work was conceived and supervised by W.P.

## Appendix A: Experimental methods

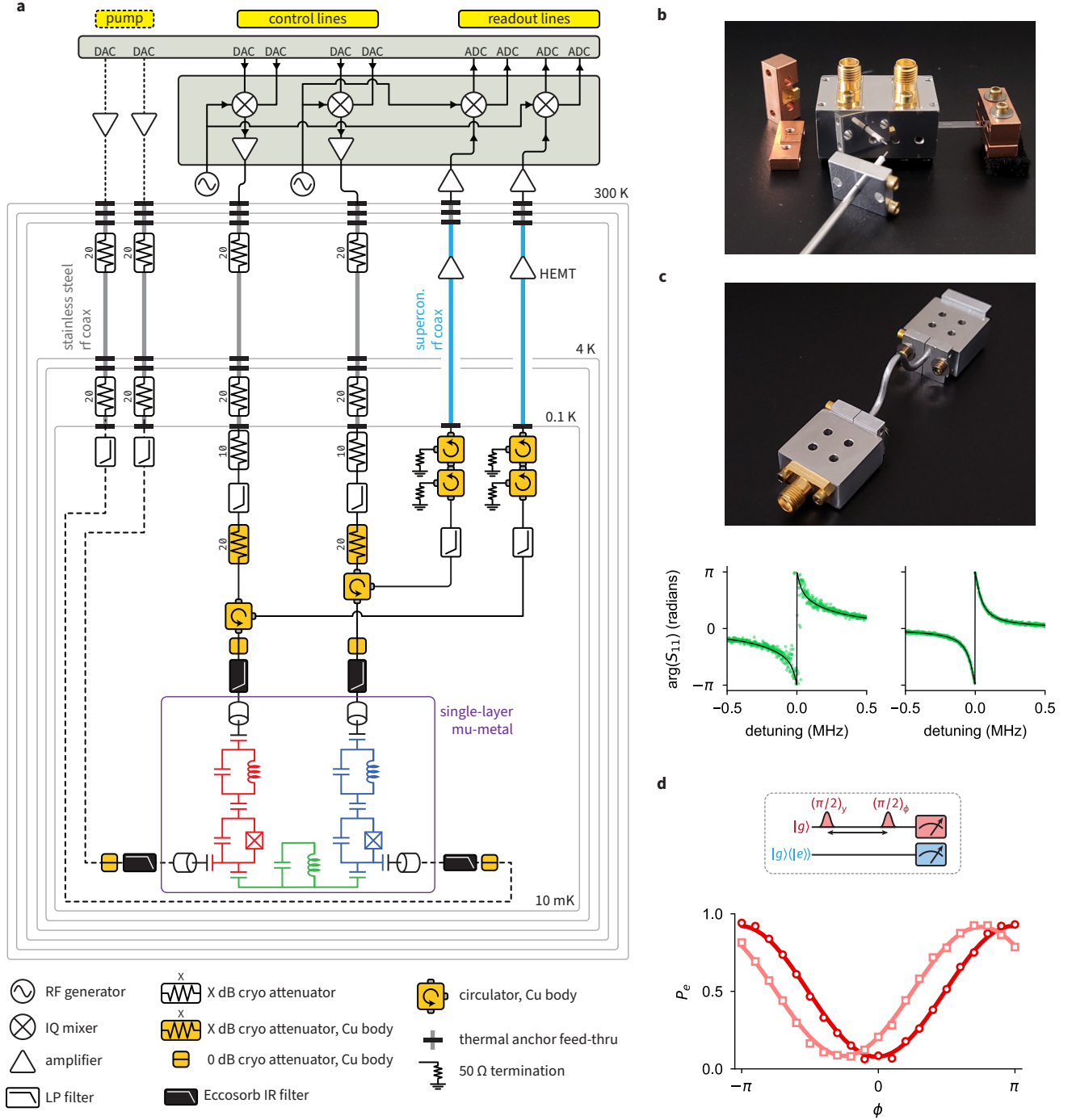
### 1. Setup

*Cryogenic measurement setup* Devices were cooled to 10 mK in an *Oxford Instruments Triton 500* dilution refrigerator. A schematic of setup and device wiring is shown in Figure 5a.

*Qubit devices* Qubit and readout resonator fabrication, as well as the basic package design follows [26]. An exploded view of a device is shown in Figure 5b. Here, the body of the sub-cutoff waveguide enclosure is made of 6061 aluminum alloy. Material choices and device fabrication limit qubit relaxation times to around 100  $\mu$ s, obtained from simulations and control devices.

*Cable assembly and characterization* Cables are clamped by Al brackets (see Fig. 1b and Fig. 5b). At the ends of the cable the outer conductor was removed with a razor blade to realize a capacitive coupling between transmon pad and inner conductor [57]. To obtain good superconducting contact, brackets and device packages were mirror-polished on a granite block, submerged in soapy water, with up to 4000-grit sandpaper. We characterized the assembly in a test setup that allows direct measurement of bus modes using a vector network analyzer (VNA), see Figure 5c. Al cables used in the network were 2.2 mm Al-PTFE-Al coaxial cable ordered from *Nanjing HMC System Co.* Initial tests on similar cables obtained from *Microcoax* showed similar performance; we were not able to source these cables anymore after initial measurements. In the network presented in the main text, the length of the cable is 73 mm, with a free spectral range (FSR) of about 1.3 GHz. The cable was chosen to be short for economical reasons; at the initial project stage we faced difficulties sourcing suitable cables. The only requirement for our experiment to work is that  $\Omega$  is much smaller than the FSR.

*Network characterization* System parameters for qubits, bus mode, and dispersive interactions are listed in Table I. The cross-Kerr between each qubit and the bus is found by measuring the qubit frequency before and after swapping an excitation into the bus [14]. The cross-Kerr term  $\chi_{a_1 a_2}$  between the qubits shown in Table I is found using Ramsey fringes (Fig. 5d).



Qubit $a_1$		Value
Mode frequency	$\omega_{a_1}/2\pi$	4675.5 MHz
Relaxation time	$T_1$	62(28) $\mu$ s
Ramsey decay	$T_{2R}$	22(1) $\mu$ s
Hahn echo decay	$T_{2E}$	34(2) $\mu$ s
Qubit $a_2$		Value
Mode frequency	$\omega_{a_2}/2\pi$	5510.7 MHz
Relaxation time	$T_1$	25(1) $\mu$ s
Ramsey decay	$T_{2R}$	8(3) $\mu$ s
Hahn echo decay	$T_{2E}$	20(1) $\mu$ s
Bus $b$		Value
Mode frequency	$\omega_b/2\pi$	5173.1 MHz
Relaxation time	$\tau_b$	6.2(2) $\mu$ s
Cross-Kerr		Value
Qubit $a_1$ and bus	$\chi_{a_1 b}/2\pi$	3.0 MHz
Qubit $a_2$ and bus	$\chi_{a_2 b}/2\pi$	9.2 MHz
Qubits $a_1$ and $a_2$	$\chi_{a_1 a_2}/2\pi$	8.0 kHz

TABLE I. **System parameters.** Mode frequencies, lifetimes, and interaction strengths for the left qubit ( $a_1$ ), right qubit ( $a_2$ ), and bus mode ( $b$ ). Uncertainties in the relaxation and coherence times reflect the fluctuations over the course of the experiment (about 3 months). Target  $\chi$  values for qubit-cable coupling was 2 MHz. Qubit coherence times were lower and fluctuate more strongly than in non-network packages. Typical  $T_{1,2}$  times in qubits made in the same way but in packages without cable mount are reliably in the 50  $\mu$ s to 100  $\mu$ s range, limited by fabrication and and sample holder material.

## 2. Data analysis

**SPAM errors** The experiments reported were conducted without using a parametric amplifier, and thus relatively low state assignment fidelity ( $P_{a_1}(g|g) = 98.5(5)\%$ ,  $P_{a_1}(e|e) = 96.0(8)\%$ ;  $P_{a_2}(g|g) = 99.3(3)\%$ ,  $P_{a_2}(e|e) = 92.3(9)\%$ ). For that reason, population data presented in the main text (with the exception of Fig. 3b) were corrected for state preparation and measurement (SPAM) errors. To perform the correction, each measurement is preceded by a calibration in which the qubits are measured after preparation in  $|g\rangle$  and  $|e\rangle$ . We used a *KMeans* clustering algorithm [58] to obtain misassignment probabilities, and then performed readout correction using that information [59, 60]. To ensure good state preparation, all qubit gates were characterized regularly using interleaved randomized benchmarking (IRB). All single-qubit gates were tuned to achieve sub-percent errors; the errors obtained are consistent with being coherence-limited. This IRB characterization ensures a small systematic error in population data. We note, however, that the central figures of merit reported are obtained from measuring decay curves that are insensitive to SPAM.

**Uncertainties and error bars** All population data shown are the mean readout signal after SPAM calibration. Statistical uncertainty on the excited state population depends on the number of samples taken and was inferred by bootstrapping state assignment and read-

out correction. For population data points without error bars, uncertainty is smaller than the marker size. To place uncertainties on the figures of merit we have employed bootstrapping as well. Raw data were randomly sub-sampled and analysis was performed for each subset. Mean and uncertainty are obtained from the distribution of outcomes in the bootstrapped analysis.

## Appendix B: Sidebands

### 1. Theoretical model

The dispersive Hamiltonian for a transmon ( $\hat{a}$ ) coupled to a microwave resonator ( $\hat{b}$ ) is given by (setting  $\hbar \equiv 1$ )

$$H = \omega_a \hat{a}^\dagger \hat{a} + \omega_b \hat{b}^\dagger \hat{b} - E_J \left( \cos(\varphi) + \frac{\varphi^2}{2} \right) \quad (\text{B1})$$

where  $\omega_a$  and  $\omega_b$  are the transmon and resonator frequencies, respectively. The phase across the Josephson junction  $\varphi = \varphi_a(\hat{a}^\dagger + \hat{a}) + \varphi_b(\hat{b}^\dagger + \hat{b})$  contains contributions from both the transmon and resonator modes, allowing for wave mixing. We then apply two microwave pump tones to the transmon, described by the additional Hamiltonian term:

$$H_{\text{pump}} = \sum_{i=1}^2 \epsilon_i (\hat{a}^\dagger e^{-i\omega_i t} + \hat{a} e^{i\omega_i t}) \quad (\text{B2})$$

where  $\epsilon_i$  is the amplitude of the pump tone and  $\omega_i$  is its frequency. Following the standard procedure (see, e.g., [16]), we move to a displaced frame for each pump tone, with displacements  $\xi_i = (\epsilon_i e^{-i\omega_i t}) / (\omega_a - \omega_i)$ , and to a rotating frame for both modes  $\hat{a}$  and  $\hat{b}$ . After expanding the transformed Hamiltonian up to fourth order we can isolate the swap term  $\propto \hat{a}^\dagger \hat{b}$  with coefficient

$$\Omega/2 = E_J \varphi_a^2 \varphi_b^2 e^{i(\omega_a - \omega_b)t} \times ((\xi_1^2 + \xi_1^{*2})/2 + (\xi_2^2 + \xi_2^{*2})/2 + \xi_1^* \xi_2 + \xi_2^* \xi_1). \quad (\text{B3})$$

This term averages out in the rotating wave approximation (RWA), unless the frequency matching condition  $\omega_2 \pm \omega_1 = |\omega_a - \omega_b|$  is satisfied. Having  $\omega_2 - \omega_1 = |\omega_a - \omega_b|$  results in the  $\xi_1^* \xi_2 + \xi_2^* \xi_1$  terms surviving the RWA. However, having  $\omega_2 + \omega_1 = |\omega_a - \omega_b|$  such that  $\omega_1 = \omega_2 = (\omega_a - \omega_b)/2$  results in all terms in Equation (B3) surviving the RWA, increasing the coefficient by a factor of two. In other words, for the degenerate case we expect twice the sideband rate for a fixed number of pump photons compared to the nondegenerate case. Given that increasing pump power results in detrimental effects [38], achieving the desired dynamics with the lowest amount of power is highly desirable. This is a primary motivation for using the low frequency parametric pumps employed in the experiment.



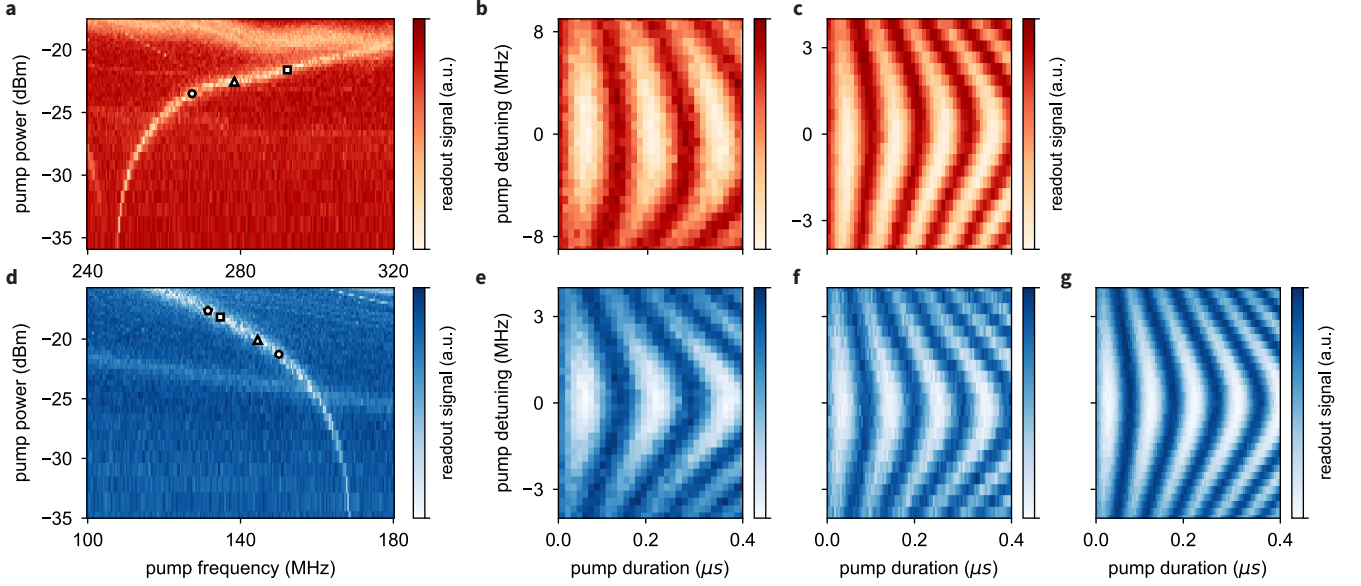


FIG. 6. **Sideband spectroscopy and additional time-domain measurements.** **a,d**, Excited state population of qubits 1 (red) and 2 (blue) as a function of frequency and device input power of the microwave drives. Markers indicate where time-domain data was taken. Circles:  $\Omega/2\pi \approx 5$  MHz (Fig. 2c,d). Triangles:  $\Omega/2\pi \approx 7$  MHz (b,e). Squares:  $\Omega/2\pi \approx 10$  MHz (c,f). Pentagon:  $\Omega/2\pi \approx 11$  MHz (g). Qubit 1 displays additional transition(s) crossing the sideband resonance near the triangle marker, resulting in a broadened and asymmetric oscillation pattern (note the different scale on the detuning axis in b).

## 2. Tuneup and limitations

Sideband oscillations for different pump powers are shown in Figure 6. The resonances shift as a function of applied power due to Stark shifts on qubit and bus,  $-\delta_a \hat{a}^\dagger \hat{a}$  and  $-\delta_b \hat{b}^\dagger \hat{b}$  respectively, where  $\delta_i$  is proportional to the pump power applied. While for qubit 2 ‘clean’ oscillations above 10 MHz can be induced, we observe distorted oscillations above 5 MHz for qubit 1. At this moment we have no explanation for the features besides the sideband resonance that appear to cause the qubit state to change. It is an outstanding question whether additional degrees of freedom (such as coupling to uncontrolled TLS) are needed to explain these features, or whether they are a result from strong-driving behavior of the transmon itself [38].

## Appendix C: Interchip gates

### 1. Prediction of SWAP efficiency

Here we describe how the calculations resulting in Figure 1d were performed. We consider the general case with the Raman drives being detuned by  $\Delta$ ,

$$H = \frac{\Omega}{2} (\hat{a}_1^\dagger \hat{b} + \hat{a}_1 \hat{b}^\dagger) + \frac{\Omega}{2} (\hat{a}_2^\dagger \hat{b} + \hat{a}_2 \hat{b}^\dagger) + \Delta \hat{b}^\dagger \hat{b}. \quad (\text{C1})$$

Increasing the detuning increases the time it takes to fully swap an excitation between the qubits. This swap

time can be found by considering the beam splitter angle, which measures how much of an excitation is transferred between qubits while leaving the bus unpopulated after the beam splitter [57]. The beam splitter angle is

$$\theta = \frac{\pi}{2} \left( 1 - \frac{\Delta}{\sqrt{8(\Omega/2)^2 + \Delta^2}} \right), \quad (\text{C2})$$

where  $\theta = \pi/2$  corresponds to a full excitation swap.  $\Omega$  is the usual sideband Rabi rate between each qubit and the bus. Next, the beam splitter time ( $\tau_{\text{BS}}$ ), the time between instances when there is no photon population in the bus, can be written as

$$\tau_{\text{BS}} = \frac{2\pi}{\sqrt{8(\Omega/2)^2 + \Delta^2}}. \quad (\text{C3})$$

To perform a full excitation swap, one can execute  $N$  beam splitter operations with angle  $\theta = \pi/2N$ , where  $N$  is a positive integer  $\geq 1$ . Note that it follows that for a given  $\Omega$ , only certain  $\Delta$  can be used to execute a full swap. The swap time can be determined as  $\tau_{\text{SWAP}} = N\tau_{\text{BS}}$ . To obtain valid swap times in Figure 1d we have fixed  $\Omega$ , and then for each  $N$  found (the unique)  $\Delta$  and  $\tau_{\text{SWAP}}$  for a single excitation swap. From there, the swap efficiency is determined by numerically evaluating the Lindblad master equation using the Hamiltonian in Eq. (C1) for a given swap time, bus quality factor  $Q_b$ , and sideband Rabi rate  $\Omega$ .

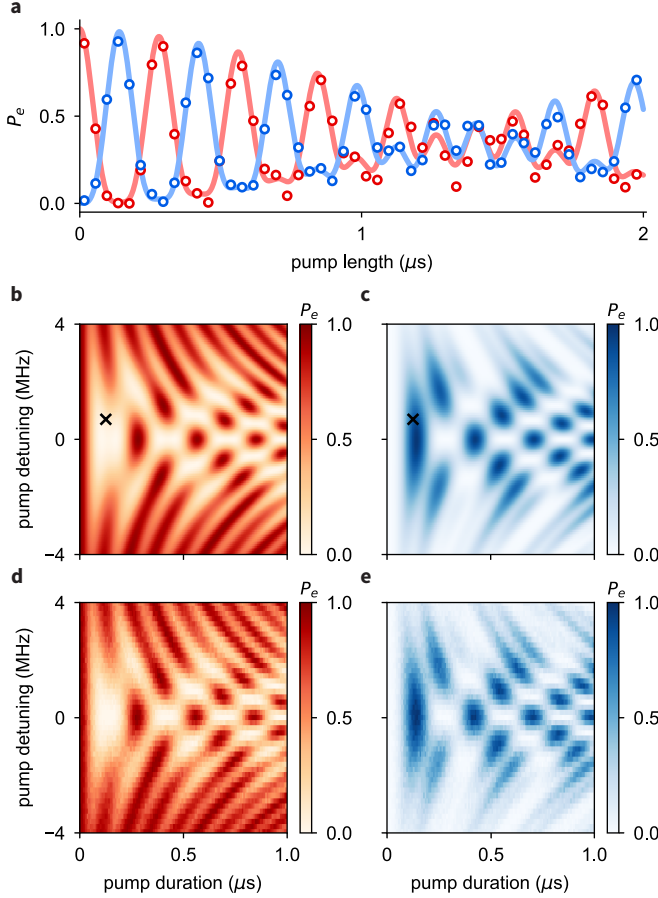


FIG. 7. **Time-dynamics of resonant Raman transitions.** **a**, Raman transitions between the qubits  $a_1$  (red) and  $a_2$  (blue), immediately after tuning both sidebands individually to 5 MHz. The simulation (solid lines) matches the data (circles) with a 0.36 MHz detuning term on the bus (Eq. (C1)). **b,c**, Simulation of the excited state population for qubits 1 (red) and 2 (blue) as a function of the drive detuning and time, assuming tuned up sidebands and no bus detuning. **d,e**, Data for the detuned swaps for the left and right qubit. In the simulation plots, ‘X’ marks a point of interest: in ref. [14] this point corresponds to an entangling gate. Here, we only predict a concurrence of 0.91 at this point, lower than what can be achieved using the stroboscopic approach shown in Fig. 3e of the main text.

## 2. Resonant Raman transitions

*Tuneup of continuous evolution* Here we describe how the system was tuned to obtain the data in Figure 3a. Each sideband is first tuned separately to a specified value of  $\Omega$  (here, 5 MHz). When both pumps are on, the total Stark shift is different compared to individual pumps, creating a mismatch in Rabi rates. Figure 7a shows continuous evolution after each sideband was only tuned individually. To restore matching we perform an iterative procedure to match the evolution to the predicted one. We evaluate the RMS error of mismatch

between data and expected ground/excited state populations for both qubits at multiples of the expected swap time,  $\tau_{\text{SWAP}} = \sqrt{2}\pi/\Omega$ . This error is minimized by iteratively tuning both pump frequencies and amplitudes. Tuneup is finished when the error converges near a minimum error or if the error is smaller than a preset threshold. Successful tuneup can be confirmed by measuring the full time evolution of both qubit state populations as a function of the drive detuning and comparing to simulation (Fig. 7b-e).

*Analysis of continuous Raman transitions* To determine the loss per swap when using continuous drives, we find the excited state probability  $P_e$  by fitting to the following equation:

$$P_e = P_e(0) \left[ e^{-t/\tau} \cos\left(\frac{\tilde{\Omega}t}{2\sqrt{2}} + \phi\right) + \frac{1}{2}(1 - e^{-t/\tau}) \right]^2, \quad (\text{C4})$$

where

$$\tilde{\Omega} = \Omega \sqrt{1 - \left(\frac{2}{\sqrt{2}\Omega\tau}\right)^2}. \quad (\text{C5})$$

$\Omega$  is the sideband Rabi rate,  $\phi$  a phase offset, and  $\tau$  is the decay time of the envelope for the swaps [57]. In an ideal system with matched Rabi rates and loss only coming from the bus,  $\tau$  should be twice the bus lifetime. The swap time is then divided by the decay time  $\tau$  to give us the percent loss per swap. From fitting the data to Eq. (C4), for qubit  $a_1$ ,  $\Omega/2\pi = 5.040(1)$  MHz and  $\tau = 14.2(7)$   $\mu\text{s}$ . For qubit  $a_2$ ,  $\Omega/2\pi = 5.041(2)$  MHz, and  $\tau = 13.3(4)$   $\mu\text{s}$ . For a Rabi rate of 5.04 MHz the swap time is 140.3 ns. To verify these results and to obtain a best estimate for our loss per swap, we have simulated the time dynamics, factoring in the measured coherence times. From simulation we obtain a decay time of 12.4(4)  $\mu\text{s}$ , twice the average bus lifetime recorded in Table I. This is the solid curve shown in Figure 3a, in very good agreement with experimental data. From this simulation, the loss per swap is 0.97(2)%.

*Tuneup of pulsed swaps* As described above, swap time is inferred from analysis of the continuous evolution. The simplest way to apply a SWAP gate is to play a rectangular pulse for this time. However, smoothed pulse edges are required to constrain the pulse bandwidth. We have shaped gate pulses as (Fig. 8a)

$$\left[ 1 + \tanh\left(\frac{2(t - \tilde{t})}{\sigma}\right) \tanh\left(\frac{2(-t + (T - \tilde{t}))}{\sigma}\right) \right] / 2 \quad (\text{C6})$$

where  $\tilde{t} = (T - t_{\text{eff}})/2$ .  $T$  is the total length given for the pulse, and  $\sigma$  is half the total time of the smooth edges on either side of the flattop pulse.  $t_{\text{eff}}$  is the effective length of the pulse such that it has the same area under it as a rectangular pulse with the same length and amplitude. Optimization of the gate is achieved by varying  $t_{\text{eff}}$ .

*Stroboscopic entanglement tune up* To tune up the sideband gate pulses used for entanglement, first each

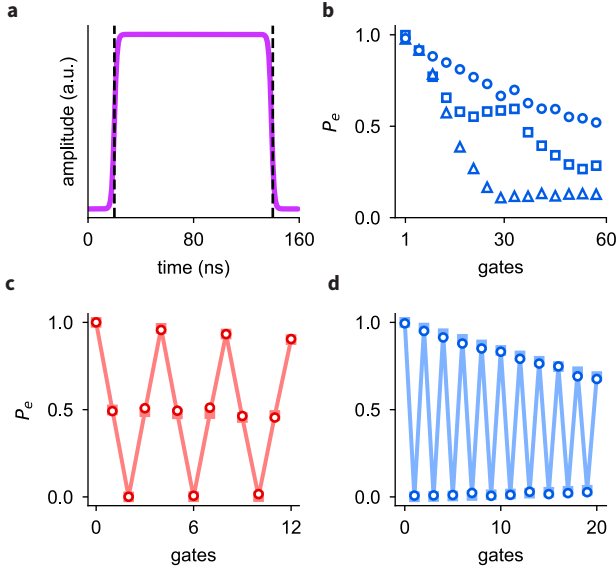


FIG. 8. **Tuning up gates between qubits.** **a**, Example of a smooth pulse used to generate the swap gate. For this pulse shown,  $T = 160$  ns,  $t_{\text{eff}} = 120$  ns, and  $\sigma = 4$  ns. Black dashed lines represent the effective gate time length. **b**, Excited state population for the right qubit as a function of consecutive gates for different effective gate times. Triangles, squares, and circles correspond to effective gate times of 139, 139.5, and 141.5 ns, respectively. Here, the 141.5 ns gate is best, as the exponential decay is indicative of least residual coherent error. **c,d**, excited state population for qubit  $a_1$  (red) and  $a_2$  (blue) as a function of the sideband gates applied where  $\Omega/2\pi \approx 5$  MHz. Circles are data, squares are from simulation. Half-swap pulses are tuned between qubit  $a_1$  and bus, full-swap pulses between bus and qubit  $a_2$ . The optimal effective sideband gate times for the left and right qubits are 52.6 ns and 101.8 ns, respectively.

sideband is set to a desired Rabi rate  $\Omega$ , and then the swap time into the bus is found simply by  $2\pi/\Omega$ . From there, we shape the sideband gates as smooth, flat-top pulses (Fig. 8a) and begin tuning over the effective sideband gate time to find the highest fidelity swap into the bus. This can be done by looking at the excited state population after a train of sideband pulses (Fig. 8c,d). The error per swap is minimized through the effective gate time. To quantify the error we take the RMS error of deviation from the ideal population (ground or excited state, alternately) and fit to an exponential decay.

### 3. Detuned Raman transitions

*Large detuning model* Treating both qubits in the frame rotating at the frequency of their corresponding pump tones, the Hamiltonian is

$$H_{\text{sys}} = \Delta \hat{a}_1^\dagger \hat{a}_1 + (\Delta - \delta) \hat{a}_2^\dagger \hat{a}_2 + \frac{\Omega}{2} (\hat{a}_1^\dagger \hat{b} + \hat{a}_2^\dagger \hat{b} + \text{h.c.}). \quad (\text{C7})$$

To simplify this Hamiltonian, we apply a Schrieffer-Wolff transformation [61]. Since  $\Omega \ll \Delta$ , we treat the mode couplings as a perturbation, and write the Hamiltonian as:

$$H_{\text{sys}} = H_{\text{sys}}^0 + V, \quad (\text{C8})$$

where  $H_{\text{sys}}^0 = \Delta \hat{a}_1^\dagger \hat{a}_1 + (\Delta - \delta) \hat{a}_2^\dagger \hat{a}_2$  and  $V = \frac{\Omega}{2} (\hat{a}_1^\dagger \hat{b} + \hat{a}_2^\dagger \hat{b} + \text{h.c.})$ . Up to the first order in  $V$ , the transformed Hamiltonian in the dressed basis is now:

$$\begin{aligned} \bar{H}_{\text{sys}} = & \Delta \left(1 + \frac{\Omega^2}{4\Delta^2}\right) \hat{a}_1^\dagger \hat{a}_1 + (\Delta - \delta) \left(1 + \frac{\Omega^2}{4(\Delta - \delta)^2}\right) \hat{a}_2^\dagger \hat{a}_2 \\ & + \frac{\Omega^2}{2} \left( \frac{1}{2\Delta} + \frac{1}{2(\Delta - \delta)} \right) (-\hat{b}^\dagger \hat{b} + \hat{a}_1^\dagger \hat{a}_2 + \hat{a}_1 \hat{a}_2^\dagger). \end{aligned} \quad (\text{C9})$$

Given that  $\Delta$  and  $(\Delta - \delta) \gg \Omega$ , we can omit the linear terms of the system.

*Dual-rail qubit tune up* We implement the detuned Raman process near 5 MHz qubit-swap rate. We detune the pump on qubit  $a_1$  by 20 MHz ( $\Delta/2\pi = 20$  MHz), and perform two-tone spectroscopy on qubit  $a_1$  while sweeping the pump frequency of qubit  $a_2$  until an avoided crossing pattern is found. The initialization of the logical qubit ( $|gg\rangle \rightarrow |0\rangle_L$  or  $|1\rangle_L$ ) is realized by local single-qubit gates, while its manipulation is implemented via detuned Raman drives. The dual-rail qubit  $\pi$  pulse is tuned up by finding the pump duration that fully swaps the excitation from one physical qubit to another. To do so, we first initialize the dual-rail qubit in the  $|0\rangle_L$  state, then turn on both of the pumps at the frequency matched point (i.e.,  $\delta = 0$ ) while sweeping the pump duration. We fit the error (residual  $|0\rangle_L$  population) near the full swap point to a quadratic model and identify the optimal duration. The  $\pi/2$  pulse is implemented by applying pumps with half the length of the  $\pi$  pulse.

*Frame evolution* The dual-rail qubit will leave the rotating frame when no pulses are applied, and will accumulate a relative phase between  $|0\rangle_L$  and  $|1\rangle_L$  at the rate of the pump frequency detuning  $\Delta$ . The Echo measurement allows for extracting this detuning quantitatively, and specifically in our case,  $\Delta/2\pi = 31.43$  MHz. This deviates from the initial setting of 20 MHz, which we attribute to the pump induced Stark shift. We can estimate the qubit-bus coupling strength by applying this value to the model that fits the time evolution data (Fig. 4c); we get  $\Omega/2\pi = \sqrt{\Omega_R \Delta}/2\pi \simeq 6.6$  MHz, which is close to our starting point, 5 MHz. We attribute this difference to the variations in the effective parametric pumping strength at different pump frequencies.

### Appendix D: Repeatability

Figure 9 shows qubit coherence times, dispersive shifts between the qubit and bus, and the bus lifetimes for a total of 13 different mounting cycles across five different samples. Cycles consisted of mounting the bus to

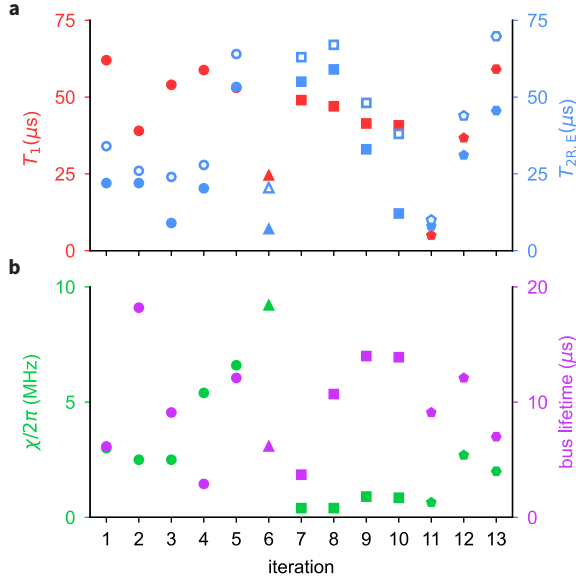


FIG. 9. **Repeatability measurements.** Each iteration is a separate cycle of a bus re-mounted to a qubit package, cooled down and measured. Exception is iteration 8, where the device was not disassembled and reassembled from iteration 7, but only thermally cycled. Different markers represent different qubit samples and packages. Together, iterations 1 and 6 are the ones during which the main experiment data was collected. We have obtained ‘clean’ Sideband oscillations with  $\Omega/2\pi \geq 5$  MHz in all iterations but iterations 7 and 8; there, we achieved only  $\Omega/2\pi \approx 4.5$  MHz before observing high-power effects. **a**, Relaxation times (solid red), Ramsey (solid blue), and echo decay times (open blue). **b**, Qubit-bus dispersive shift  $\chi$  (green) and bus lifetime (purple) across each iteration.

a package containing a qubit, cooling to base temperature and performing measurements, warming up, removing and re-attaching the bus. Importantly, we were able to reach  $\Omega/2\pi \geq 5$  MHz sidebands in 11 out of these 13 iterations. This indicates that while our mounting system is simple, it already allows for a reliable interconnect. The wide spread of system parameters across these cycles is, however, noteworthy and points toward the need for improved mechanical designs. In particular, coherence times are shorter and vary more than typical devices without the mounted cable in our lab; typical coherence times in similar packages but without cable mounts reach routinely 50  $\mu s$  to 100  $\mu s$ , limited by the single-step fabrication process used here and by the material of the qubit packages. We believe that the mechanics of the mount need to be improved before state-of-the-art coherence in these types of packages [33] can be reached in combination with cable mounts. As for the dispersive interaction between the transmon and cable bus mode, the design value is  $\chi/2\pi = 2$  MHz, but the measured spread is 0.4 MHz to 9.2 MHz. From finite-element simulations we have found that this can be explained by a variation of inner-conductor to chip distance up  $\pm 0.5$  mm from the target position. This variation is, given the softness of Al cable, a realistic run-to-run spread.

- 
- [1] H. J. Kimble, The quantum internet, *Nature* **453**, 1023 (2008).
  - [2] C. Monroe, R. Raussendorf, A. Ruthven, K. R. Brown, P. Maunz, L.-M. Duan, and J. Kim, Large-scale modular quantum-computer architecture with atomic memory and photonic interconnects, *Physical Review A* **89**, 022317 (2014).
  - [3] D. Awschalom, K. K. Berggren, H. Bernien, S. Bhawe, L. D. Carr, P. Davids, S. E. Economou, D. Englund, A. Faraon, M. Fejer, S. Guha, M. V. Gustafsson, E. Hu, L. Jiang, J. Kim, B. Korzh, P. Kumar, P. G. Kwiat, M. Lončar, M. D. Lukin, D. A. Miller, C. Monroe, S. W. Nam, P. Narang, J. S. Orcutt, M. G. Raymer, A. H. Safavi-Naeini, M. Spiropulu, K. Srinivasan, S. Sun, J. Vučković, E. Waks, R. Walsworth, A. M. Weiner, and Z. Zhang, Development of Quantum Interconnects (QulCs) for Next-Generation Information Technologies, *PRX Quantum* **2**, 017002 (2021).
  - [4] J. Ang, G. Carini, Y. Chen, I. Chuang, M. A. DeMarco, S. E. Economou, A. Eickbusch, A. Faraon, K.-M. Fu, S. M. Girvin, M. Hatridge, A. Houck, P. Hilaire, K. Kruslich, A. Li, C. Liu, Y. Liu, M. Martonosi, D. C. McKay, J. Misewich, M. Ritter, R. J. Schoelkopf, S. A. Stein, S. Sussman, H. X. Tang, W. Tang, T. Tomesh, N. M. Tubman, C. Wang, N. Wiebe, Y.-X. Yao, D. C. Yost, and Y. Zhou, Architectures for Multinode Superconducting Quantum Computers (2022), [arXiv:2212.06167 \[quant-ph\]](https://arxiv.org/abs/2212.06167).
  - [5] S. Bravyi, O. Dial, J. M. Gambetta, D. Gil, and Z. Nazario, The future of quantum computing with superconducting qubits, *Journal of Applied Physics* **132**, 160902 (2022).
  - [6] K. N. Smith, G. S. Ravi, J. M. Baker, and F. T. Chong, Scaling Superconducting Quantum Computers with Chiplet Architectures, in *2022 55th IEEE/ACM International Symposium on Microarchitecture (MICRO)* (IEEE, Chicago, IL, USA, 2022) pp. 1092–1109.
  - [7] N. Roch, M. E. Schwartz, F. Motzoi, C. Macklin, R. Vijay, A. W. Eddins, A. N. Korotkov, K. B. Whaley, M. Sarovar, and I. Siddiqi, Observation of Measurement-Induced Entanglement and Quantum Trajectories of Remote Superconducting Qubits, *Physical Review Letters* **112**, 170501 (2014).
  - [8] C. Dickel, J. J. Westdorp, N. K. Langford, S. Peiter, R. Sagastizabal, A. Bruno, B. Criger, F. Motzoi, and L. DiCarlo, Chip-to-chip entanglement of transmon



- qubits using engineered measurement fields, *Physical Review B* **97**, 064508 (2018).
- [9] A. Narla, S. Shankar, M. Hatridge, Z. Leghtas, K. M. Sliwa, E. Zalus-Geller, S. O. Mundhada, W. Pfaff, L. Frunzio, R. J. Schoelkopf, and M. H. Devoret, Robust Concurrent Remote Entanglement Between Two Superconducting Qubits, *Physical Review X* **6**, 031036 (2016).
  - [10] N. Leung, Y. Lu, S. Chakram, R. K. Naik, N. Earnest, R. Ma, K. Jacobs, A. N. Cleland, and D. I. Schuster, Deterministic bidirectional communication and remote entanglement generation between superconducting qubits, *npj Quantum Information* **5**, 1 (2019).
  - [11] Y. Zhong, H.-S. Chang, A. Bienfait, É. Dumur, M.-H. Chou, C. R. Conner, J. Grebel, R. G. Povey, H. Yan, D. I. Schuster, and A. N. Cleland, Deterministic multi-qubit entanglement in a quantum network, *Nature* **590**, 571 (2021).
  - [12] J. Niu, L. Zhang, Y. Liu, J. Qiu, W. Huang, J. Huang, H. Jia, J. Liu, Z. Tao, W. Wei, Y. Zhou, W. Zou, Y. Chen, X. Deng, X. Deng, C. Hu, L. Hu, J. Li, D. Tan, Y. Xu, F. Yan, T. Yan, S. Liu, Y. Zhong, A. N. Cleland, and D. Yu, Low-loss interconnects for modular superconducting quantum processors, *Nature Electronics* **6**, 235 (2023).
  - [13] J. Qiu, Y. Liu, J. Niu, L. Hu, Y. Wu, L. Zhang, W. Huang, Y. Chen, J. Li, S. Liu, Y. Zhong, L. Duan, and D. Yu, Deterministic quantum teleportation between distant superconducting chips (2023), [arXiv:2302.08756](https://arxiv.org/abs/2302.08756) [quant-ph].
  - [14] L. D. Burkhardt, J. D. Teoh, Y. Zhang, C. J. Axline, L. Frunzio, M. Devoret, L. Jiang, S. Girvin, and R. Schoelkopf, Error-Detected State Transfer and Entanglement in a Superconducting Quantum Network, *PRX Quantum* **2**, 030321 (2021).
  - [15] P. Kurpiers, P. Magnard, T. Walter, B. Royer, M. Pechal, J. Heinsoo, Y. Salathé, A. Akin, S. Storz, J.-C. Besse, S. Gasparinetti, A. Blais, and A. Wallraff, Deterministic quantum state transfer and remote entanglement using microwave photons, *Nature* **558**, 264 (2018).
  - [16] P. Campagne-Ibarcq, E. Zalus-Geller, A. Narla, S. Shankar, P. Reinhold, L. Burkhardt, C. Axline, W. Pfaff, L. Frunzio, R. J. Schoelkopf, and M. H. Devoret, Deterministic Remote Entanglement of Superconducting Circuits through Microwave Two-Photon Transitions, *Physical Review Letters* **120**, 200501 (2018).
  - [17] C. J. Axline, L. D. Burkhardt, W. Pfaff, M. Zhang, K. Chou, P. Campagne-Ibarcq, P. Reinhold, L. Frunzio, S. M. Girvin, L. Jiang, M. H. Devoret, and R. J. Schoelkopf, On-demand quantum state transfer and entanglement between remote microwave cavity memories, *Nature Physics* **14**, 705 (2018).
  - [18] C. Zhou, P. Lu, M. Praquin, T.-C. Chien, R. Kaufman, X. Cao, M. Xia, R. S. K. Mong, W. Pfaff, D. Pekker, and M. Hatridge, Realizing all-to-all couplings among detachable quantum modules using a microwave quantum state router, *npj Quantum Information* **9**, 1 (2023).
  - [19] J. Ramette, J. Sinclair, N. P. Breuckmann, and V. Vuletić, Fault-tolerant connection of error-corrected qubits with noisy links, *npj Quantum Information* **10**, 1 (2024).
  - [20] A. Gold, J. P. Paquette, A. Stockklauser, M. J. Reagor, M. S. Alam, A. Bestwick, N. Didier, A. Nersisyan, F. Oruc, A. Razavi, B. Scharmann, E. A. Sete, B. Sur, D. Venturelli, C. J. Winkleblack, F. Wudarski, M. Harburn, and C. Rigetti, Entanglement across separate silicon dies in a modular superconducting qubit device, *npj Quantum Information* **7**, 142 (2021).
  - [21] C. R. Conner, A. Bienfait, H.-S. Chang, M.-H. Chou, É. Dumur, J. Grebel, G. A. Peairs, R. G. Povey, H. Yan, Y. P. Zhong, and A. N. Cleland, Superconducting qubits in a flip-chip architecture, *Applied Physics Letters* **118**, 232602 (2021).
  - [22] A. G. Fowler, A. M. Stephens, and P. Groszkowski, High-threshold universal quantum computation on the surface code, *Physical Review A* **80**, 052312 (2009).
  - [23] R. Barends, J. Kelly, A. Megrant, A. Veitia, D. Sank, E. Jeffrey, T. C. White, J. Mutus, A. G. Fowler, B. Campbell, Y. Chen, Z. Chen, B. Chiaro, A. Dunsworth, C. Neill, P. O'Malley, P. Roushan, A. Vainsencher, J. Wenner, A. N. Korotkov, A. N. Cleland, and J. M. Martinis, Superconducting quantum circuits at the surface code threshold for fault tolerance, *Nature* **508**, 500 (2014).
  - [24] P. Kurpiers, T. Walter, P. Magnard, Y. Salathe, and A. Wallraff, Characterizing the attenuation of coaxial and rectangular microwave-frequency waveguides at cryogenic temperatures, *EPJ Quantum Technology* **4**, 8 (2017), [arXiv:1612.07977](https://arxiv.org/abs/1612.07977).
  - [25] J. Majer, J. M. Chow, J. M. Gambetta, J. Koch, B. R. Johnson, J. A. Schreier, L. Frunzio, D. I. Schuster, A. A. Houck, A. Wallraff, A. Blais, M. H. Devoret, S. M. Girvin, and R. J. Schoelkopf, Coupling superconducting qubits via a cavity bus, *Nature* **449**, 443 (2007).
  - [26] C. Axline, M. Reagor, R. Heeres, P. Reinhold, C. Wang, K. Shain, W. Pfaff, Y. Chu, L. Frunzio, and R. J. Schoelkopf, An architecture for integrating planar and 3D cQED devices, *Applied Physics Letters* **109**, 042601 (2016).
  - [27] J. M. Gertler, B. Baker, J. Li, S. Shirol, J. Koch, and C. Wang, Protecting a bosonic qubit with autonomous quantum error correction, *Nature* **590**, 243 (2021).
  - [28] S. Chakram, K. He, A. V. Dixit, A. E. Oriani, R. K. Naik, N. Leung, H. Kwon, W.-L. Ma, L. Jiang, and D. I. Schuster, Multimode photon blockade, *Nature Physics* **18**, 879 (2022).
  - [29] V. V. Sivak, A. Eickbusch, B. Royer, S. Singh, I. Tsioutsios, S. Ganjam, A. Miano, B. L. Brock, A. Z. Ding, L. Frunzio, S. M. Girvin, R. J. Schoelkopf, and M. H. Devoret, Real-time quantum error correction beyond break-even, *Nature* **616**, 50 (2023).
  - [30] Z. Ni, S. Li, X. Deng, Y. Cai, L. Zhang, W. Wang, Z.-B. Yang, H. Yu, F. Yan, S. Liu, C.-L. Zou, L. Sun, S.-B. Zheng, Y. Xu, and D. Yu, Beating the break-even point with a discrete-variable-encoded logical qubit, *Nature* **616**, 56 (2023).
  - [31] O. Milul, B. Guttel, U. Goldblatt, S. Hazanov, L. M. Joshi, D. Chausovsky, N. Kahn, E. Çiftçiyörek, F. Lafont, and S. Rosenblum, Superconducting Cavity Qubit with Tens of Milliseconds Single-Photon Coherence Time, *PRX Quantum* **4**, 030336 (2023).
  - [32] A. Koottandavida, I. Tsioutsios, A. Kargioti, C. R. Smith, V. R. Joshi, W. Dai, J. D. Teoh, J. C. Curtis, L. Frunzio, R. J. Schoelkopf, and M. H. Devoret, Erasure Detection of a Dual-Rail Qubit Encoded in a Double-Post Superconducting Cavity, *Physical Review Letters* **132**, 180601 (2024).

- [33] S. Ganjam, Y. Wang, Y. Lu, A. Banerjee, C. U. Lei, L. Krayzman, K. Kisslinger, C. Zhou, R. Li, Y. Jia, M. Liu, L. Frunzio, and R. J. Schoelkopf, Surpassing millisecond coherence in on chip superconducting quantum memories by optimizing materials and circuit design, *Nature Communications* **15**, 3687 (2024).
- [34] K. S. Chou, J. Z. Blumoff, C. S. Wang, P. C. Reinhold, C. J. Axline, Y. Y. Gao, L. Frunzio, M. H. Devoret, L. Jiang, and R. J. Schoelkopf, Deterministic teleportation of a quantum gate between two logical qubits, *Nature* **561**, 368 (2018).
- [35] A. Wallraff, D. I. Schuster, A. Blais, J. M. Gambetta, J. Schreier, L. Frunzio, M. H. Devoret, S. M. Girvin, and R. J. Schoelkopf, Sideband Transitions and Two-Tone Spectroscopy of a Superconducting Qubit Strongly Coupled to an On-Chip Cavity, *Physical Review Letters* **99**, 050501 (2007).
- [36] K. Bergmann, H. Theuer, and B. W. Shore, Coherent population transfer among quantum states of atoms and molecules, *Reviews of Modern Physics* **70**, 1003 (1998).
- [37] D. I. Schuster, A. A. Houck, J. A. Schreier, A. Wallraff, J. M. Gambetta, A. Blais, L. Frunzio, J. Majer, B. Johnson, M. H. Devoret, S. M. Girvin, and R. J. Schoelkopf, Resolving photon number states in a superconducting circuit, *Nature* **445**, 515 (2007).
- [38] R. Shillito, A. Petrescu, J. Cohen, J. Beall, M. Hauru, M. Ganahl, A. G. Lewis, G. Vidal, and A. Blais, Dynamics of Transmon Ionization, *Physical Review Applied* **18**, 034031 (2022).
- [39] L. V. Abdurakhimov, I. Mahboob, H. Toida, K. Kakuyanagi, Y. Matsuzaki, and S. Saito, Identification of Different Types of High-Frequency Defects in Superconducting Qubits, *PRX Quantum* **3**, 040332 (2022).
- [40] M. Xia, C. Zhou, C. Liu, P. Patel, X. Cao, P. Lu, B. Mesits, M. Mucci, D. Gorski, D. Pekker, and M. Hatridge, Fast superconducting qubit control with sub-harmonic drives (2023), [arXiv:2306.10162 \[quant-ph\]](https://arxiv.org/abs/2306.10162).
- [41] K. S. Chou, T. Shemima, H. McCarrick, T.-C. Chien, J. D. Teoh, P. Winkel, A. Anderson, J. Chen, J. C. Curtis, S. J. De Graaf, J. W. O. Garmon, B. Gudlewski, W. D. Kalfus, T. Keen, N. Khedkar, C. U. Lei, G. Liu, P. Lu, Y. Lu, A. Maiti, L. Mastalli-Kelly, N. Mehta, S. O. Mundhada, A. Narla, T. Noh, T. Tsunoda, S. H. Xue, J. O. Yuan, L. Frunzio, J. Aumentado, S. Puri, S. M. Girvin, S. H. Moseley, and R. J. Schoelkopf, A superconducting dual-rail cavity qubit with erasure-detected logical measurements, *Nature Physics* **10.1038/s41567-024-02539-4** (2024).
- [42] J. D. Teoh, P. Winkel, H. K. Babla, B. J. Chapman, J. Claes, S. J. de Graaf, J. W. O. Garmon, W. D. Kalfus, Y. Lu, A. Maiti, K. Sahay, N. Thakur, T. Tsunoda, S. H. Xue, L. Frunzio, S. M. Girvin, S. Puri, and R. J. Schoelkopf, Dual-rail encoding with superconducting cavities, *Proceedings of the National Academy of Sciences* **120**, e2221736120 (2023).
- [43] H. Levine, A. Haim, J. S. C. Hung, N. Alidoust, M. Kalaei, L. DeLorenzo, E. A. Wollack, P. Arrangoiz-Arriola, A. Khalajhedayati, R. Sanil, H. Moradinejad, Y. Vaknin, A. Kubica, D. Hover, S. Aghaeimeibodi, J. A. Alcid, C. Baek, J. Barnett, K. Bawdekar, P. Bienias, H. A. Carson, C. Chen, L. Chen, H. Chinkejian, E. M. Chisholm, A. Clifford, R. Cosmic, N. Crisosto, A. M. Dalzell, E. Davis, J. M. D'Ewart, S. Diez, N. D'Souza, P. T. Dumitrescu, E. Elkhoully, M. T. Fang, Y. Fang, S. Flammia, M. J. Fling, G. Garcia, M. K. Gharzai, A. V. Gorshkov, M. J. Gray, S. Grimberg, A. L. Grimsmo, C. T. Hann, Y. He, S. Heide, S. Howell, M. Hunt, J. Iverson, I. Jarrige, L. Jiang, W. M. Jones, R. Karabalin, P. J. Karalekas, A. J. Keller, D. Lasi, M. Lee, V. Ly, G. MacCabe, N. Mahuli, G. Maraud, M. H. Matheny, S. McArdle, G. McCabe, G. Merton, C. Miles, A. Milsted, A. Mishra, L. Moncelis, M. Naghiloo, K. Noh, E. Oblepias, G. Ortuno, J. C. Owens, J. Pagdilao, A. Panduro, J.-P. Paquette, R. N. Patel, G. Peairs, D. J. Perello, E. C. Peterson, S. Ponte, H. Putterman, G. Refael, P. Reinhold, R. Resnick, O. A. Reyna, R. Rodriguez, J. Rose, A. H. Rubin, M. Runyan, C. A. Ryan, A. Sahmoud, T. Scaffidi, B. Shah, S. Siavoshi, P. Sivaraiah, T. Skogland, C.-J. Su, L. J. Swenson, J. Sylvia, S. M. Teo, A. Tomada, G. Torlai, M. Wistrom, K. Zhang, I. Zuk, A. A. Clerk, F. G. S. L. Brandão, A. Retzker, and O. Painter, Demonstrating a Long-Coherence Dual-Rail Erasure Qubit Using Tunable Transmons, *Physical Review X* **14**, 011051 (2024).
- [44] S. J. de Graaf, S. H. Xue, B. J. Chapman, J. D. Teoh, T. Tsunoda, P. Winkel, J. W. O. Garmon, K. M. Chang, L. Frunzio, S. Puri, and R. J. Schoelkopf, *A mid-circuit erasure check on a dual-rail cavity qubit using the joint-photon number-splitting regime of circuit QED* (2024), [arXiv:2406.14621 \[quant-ph\]](https://arxiv.org/abs/2406.14621).
- [45] A. Kubica, A. Haim, Y. Vaknin, H. Levine, F. Brandão, and A. Retzker, Erasure Qubits: Overcoming the  $\{T\}_{-1}$  Limit in Superconducting Circuits, *Physical Review X* **13**, 041022 (2023).
- [46] A. P. M. Place, L. V. H. Rodgers, P. Mundada, B. M. Smitham, M. Fitzpatrick, Z. Leng, A. Premkumar, J. Bryon, A. Vrajitoarea, S. Sussman, G. Cheng, T. Madhavan, H. K. Babla, X. H. Le, Y. Gang, B. Jäck, A. Gynis, N. Yao, R. J. Cava, N. P. de Leon, and A. A. Houck, New material platform for superconducting transmon qubits with coherence times exceeding 0.3 milliseconds, *Nature Communications* **12**, 1779 (2021).
- [47] A. Somoroff, Q. Ficheux, R. A. Mencia, H. Xiong, R. Kuzmin, and V. E. Manucharyan, Millisecond Coherence in a Superconducting Qubit, *Physical Review Letters* **130**, 267001 (2023).
- [48] C. Wang, X. Li, H. Xu, Z. Li, J. Wang, Z. Yang, Z. Mi, X. Liang, T. Su, C. Yang, G. Wang, W. Wang, Y. Li, M. Chen, C. Li, K. Linghu, J. Han, Y. Zhang, Y. Feng, Y. Song, T. Ma, J. Zhang, R. Wang, P. Zhao, W. Liu, G. Xue, Y. Jin, and H. Yu, Towards practical quantum computers: Transmon qubit with a lifetime approaching 0.5 milliseconds, *npj Quantum Information* **8**, 3 (2022).
- [49] S. Kono, J. Pan, M. Chegnizadeh, X. Wang, A. Youssefi, M. Scigliuzzo, and T. J. Kippenberg, Mechanically induced correlated errors on superconducting qubits with relaxation times exceeding 0.4 ms, *Nature Communications* **15**, 3950 (2024).
- [50] A. Safwat, K. Zaki, W. Johnson, and C. Lee, Novel transition between different configurations of planar transmission lines, *IEEE Microwave and Wireless Components Letters* **12**, 128 (2002).
- [51] R. S. Beeresha, A. M. Khan, and H. V. M. Reddy, CPW to microstrip transition using different CPW ground plane structures, in *2016 IEEE International Conference on Recent Trends in Electronics, Information & Communication Technology (RTEICT)* (IEEE, Bangalore, India, 2016) pp. 667–671.

- [52] U. Vool, A. Kou, W. C. Smith, N. E. Frattini, K. Serniak, P. Reinhold, I. M. Pop, S. Shankar, L. Frunzio, S. M. Girvin, and M. H. Devoret, Driving Forbidden Transitions in the Fluxonium Artificial Atom, *Physical Review Applied* **9**, 054046 (2018).
- [53] K. Nie, A. Bista, K. Chow, W. Pfaff, and A. Kou, Parametrically-controlled microwave-photon interface for the fluxonium (2024), [arXiv:2404.11847 \[quant-ph\]](#).
- [54] D. Lachance-Quirion, S. P. Wolski, Y. Tabuchi, S. Kono, K. Usami, and Y. Nakamura, Entanglement-based single-shot detection of a single magnon with a superconducting qubit, *Science* **367**, 425 (2020).
- [55] P. Harvey-Collard, J. Dijkema, G. Zheng, A. Sammak, G. Scappucci, and L. M. K. Vandersypen, Coherent Spin-Spin Coupling Mediated by Virtual Microwave Photons, *Physical Review X* **12**, 021026 (2022).
- [56] S. Krinner, S. Storz, P. Kurpiers, P. Magnard, J. Heinsoo, R. Keller, J. Lütolf, C. Eichler, and A. Wallraff, Engineering cryogenic setups for 100-qubit scale superconducting circuit systems, *EPJ Quantum Technology* **6**, 2 (2019).
- [57] L. Burkhart, *Error-Detected Networking for 3D Circuit Quantum Electrodynamics*, Ph.D. thesis, Yale University (2020).
- [58] F. Pedregosa, G. Varoquaux, A. Gramfort, V. Michel, B. Thirion, O. Grisel, M. Blondel, P. Prettenhofer, R. Weiss, V. Dubourg, J. Vanderplas, A. Passos, D. Cournapeau, M. Brucher, M. Perrot, and E. Duchesnay, Scikit-learn: Machine learning in Python, *Journal of Machine Learning Research* **12**, 2825 (2011).
- [59] M. R. Geller and M. Sun, Toward efficient correction of multiqubit measurement errors: Pair correlation method, *Quantum Science and Technology* **6**, 025009 (2021).
- [60] J. B. Severin, *Superconducting Qubit Readout In Theory, Experiment, And Simulation*, Master's thesis, University of Copenhagen (2023).
- [61] A. Blais, A. L. Grimsmo, S. M. Girvin, and A. Wallraff, Circuit quantum electrodynamics, *Reviews of Modern Physics* **93**, 025005 (2021).